NJC

Accepted Manuscript

This is an *Accepted Manuscript*, which has been through the Royal Society of Chemistry peer review process and has been accepted for publication.

Accepted Manuscripts are published online shortly after acceptance, before technical editing, formatting and proof reading. Using this free service, authors can make their results available to the community, in citable form, before we publish the edited article. We will replace this *Accepted Manuscript* with the edited and formatted *Advance Article* as soon as it is available.

You can find more information about *Accepted Manuscripts* in the Information for Authors.

Please note that technical editing may introduce minor changes to the text and/or graphics, which may alter content. The journal's standard Terms & Conditions and the Ethical guidelines still apply. In no event shall the Royal Society of Chemistry be held responsible for any errors or omissions in this *Accepted Manuscript* or any consequences arising from the use of any information it contains.

ROYAL SOCIETY OF CHEMISTRY

www.rsc.org/njc

Cite this: DOI: 10.1039/c0xx00000x

www.rsc.org/xxxxxx

paper

$Li_4Ti_5O_{12}$–rutile TiO_2 nanocomposite with excellent high rate cycling stability for lithium-ion batteries

Xi-Ping Li and Jian Mao*

Received (in XXX, XXX) Xth XXXXXXXXX 20XX, Accepted Xth XXXXXXXXX 20XX

DOI: 10.1039/b000000x

Abstract: $Li_4Ti_5O_{12}$–rutile TiO_2 nanocomposite was synthesized by sol-hydrothermal synthesis method using $LiOH·H_2O$ and $Ti(OC_4H_9)_4$ as precursors. The obtained material exhibits a micron-sized flower-like morphology (3 μm to 4 μm) constituted by layer-stacked nanosheets. In the composite material, nanosized rutile TiO_2 sheets are in situ generated and adhered on the $Li_4Ti_5O_{12}$ sheets. These nanosized rutile TiO_2 sheets in the $Li_4Ti_5O_{12}$–rutile TiO_2 composite play important roles in producing numerous $Li_4Ti_5O_{12}$/rutile TiO_2 two-phase interfaces as tiny reaction sites for rapid lithium intercalation and extraction, inhibiting the side reactions with electrolyte, and avoiding the aggregation of primary nanosheets during the long-term cycling process. Benefiting from these unique features, the $Li_4Ti_5O_{12}$–rutile TiO_2 composite exhibits excellent rate capability (a reversible capacity of 148, 146 and 142 mA h g^{-1} at 5, 10 and 20 C, respectively, 1 C=175 mA g^{-1}) and outstanding long-term cycling stability (only 6.3% capacity loss after 1000 cycles at a high rate of 10 C).

1 Introduction

In the lithium–ion battery anode materials, the graphite has been widely used in the portable electronic products due to the advantages of flat discharge voltage, stable cyclic properties, excellent electrical conductivity and abundant resources.[1–2] However, these lithium-ion batteries containing graphite-based anodes suffer from serious safety risks, which are caused by the dendritic growth of lithium on the anode surface under the high current density due to the very low lithiation potential (close to 0 V vs. Li^+/Li) of carbon material.[3–4] Once these lithium dendrites penetrate the diaphragm, the battery will be short-circuited, causing serious safety concerns such as fire and explosion accidents[5], which limits the application in power battery for electric vehicles (EVs) and hybrid vehicles (HEVs). Therefore, searching for alternative anode materials with excellent rate-capability, good safety property, and long-term cycling stability has become an urgent problem in the high-power battery research field. Many new anode materials, including SnO_2, Li_3SbO_4, SiO_2, Fe_3O_4, ZnO, TiO_2 and $Li_4Ti_5O_{12}$, have been proposed and extensively investigated.[1-3, 6-10]

Among these materials, spinel $Li_4Ti_5O_{12}$ and anatase TiO_2 are promising anode materials that can be used as alternatives to graphite in high-power lithium–ion batteries. These low-cost and non-toxic materials exhibit excellent Li^+ intercalation/deintercalation reversibility with very minimal structural change and good safety level because of their high discharge platform caused by side reactions inhibition.[11–14] Unfortunately, these two promising anode materials suffer from poor rate capability because of their low electrical conductivity, thereby limiting their practical applications. [15–16]

Recently, two effective strategies were used to improve the rate performance of lithium–ion batteries. The first is fabrication of multinary compounds with high grain boundary density or large phase interfacial areas, because lithium ions can react reversibly with atoms at and within grain boundaries or phase interfacial areas in polycrystalline materials producing additional lithium storage.[17–18] For example, LiF-Ti,[18] Sn_2Mn-$SnMn_3C$,[19] $Li_4Ti_5O_{12}$-$Li_2Ti_3O_7$,[20] and $Li_4Ti_5O_{12}$-TiO_2 nanocomposites [11, 13, 21–24] have been reported showing a significant improvement in rate capability in comparison with that of bulk materials. The second strategy to enhance the electrochemical performance is fabricating nanosheets electrode materials, because the thin nanosheets constituents providing a short lithium diffusion path. For example, L. Yang et al. reported sawtooth-like $Li_4Ti_5O_{12}$ nanosheets, which show high reversible capacity and stable cyclic performance even at high rates.[25] D. Lou et al. reported flower-like spheres assembled from SnO_2 nanosheets exhibited fast lithium ion storage ability. [26] Han, X. G et al. using a modified hydrothermal method synthesized anatase TiO_2 nanosheets with exposed (001) high-energy facets. The as-prepared sample shows high capacity and excellent cycling stability at rates of 10 and 20 C.[27] As both methods, either fabricating multinary compound or nanosheet morphology material, result in improved electrochemical performances, therefore, it is highly desirable to develop a kind of $Li_4Ti_5O_{12}$-based nanosheet composite that combines both large interfacial areas and short lithium diffusion path.

According to previous researches,[11, 13, 21–23] dual-phase $Li_4Ti_5O_{12}$-anatase TiO_2 composites exhibit much improved rate capability in comparison with that of bulk materials. Despite this progress, this kind of composite often suffers from poor crystallinity, thus leading to fast decay of capacity after several hundred cycles. Recently, Guo et al.[28] reported a one-pot hydrothermal synthesis process for the fabrication of rutile TiO_2 coated $Li_4Ti_5O_{12}$ nanosheets at the edges, which shows a significant improvement in rate capability and specific capacity compared with pure $Li_4Ti_5O_{12}$. Besides, TiO_2 coated $Li_4Ti_5O_{12}$ nanosheets also show excellent cycling performance at high rate

of 5 C and 20 C.

Based on previous researches, [11, 13, 21–23, 28–30] in this work, we demonstrate a facile and scalable synthesis of $Li_4Ti_5O_{12}$ (LTO) and rutile TiO_2 (RTO) nanosheets assembled nanocomposite (LTO-RTO) with flower-like morphology via a sol-hydrothermal method. In the fabrication process, smaller RTO nanosheets are in situ generated and attached on the surface of LTO nanosheets, producing a great number of nanosized LTO/RTO two phase interfacial areas, which are beneficial for high rate performance of lithium ion batteries electrode. Compared with pure LTO nanosheets prepared with same procedure, LTO–RTO nanocomposite shows larger specific capacity, much better rate capability and higher cycling stability. In this article, we will discuss how the in situ generated RTO nanosheets improve the overall electrochemical performance of LTO-RTO nanocomposite.

2 Experimental

2.1 Material synthesis

All chemicals used in the experiments are analytical reagent. LTO–RTO and LTO powder samples were synthesized using LiOH·H_2O and $Ti(OC_4H_9)_4$ as starting materials. Firstly, 17 mL $Ti(OC_4H_9)_4$ was dissolved in 34 mL alcohol with stirring to form a pale yellow solution, which was marked as A. Secondly, 1.68 g LiOH·H_2O was added into 20 mL distilled water to obtain lithium hydroxide solution, which was marked as B. After that, solution B was dropwise added into the solution A with strong magnetic stirring for 0.5 h to get a white suspension, and then transferred into 100 mL stainless-steel autoclave placed in an oven at 180 ℃ for 34 h. After reaction, the precipitation deposited at the bottom of the reactor was filtered, and washed with ethanol to obtain white precursor. The obtained precursor was dried and ground. Finally, the powder was sintered at 600 ℃ for 10 h in a muffle furnace to obtain well-crystallized LTO–RTO nanosheet composite. Changing the amount of LiOH·H_2O to 1.89 g, the pure LTO was obtained with same procedure.

2.2 Material Characterization

The crystal structure of the obtained samples were characterized by powder X-ray diffraction using X'Pert Pro MPD diffraction instrument with Cu $K\alpha_1$ radiation (λ=0.154056nm) in the 2θ range of 10 to 90°. X-ray photoelectron spectroscopy (XPS) experiments were carried out on a XSAM800 instrument using aluminum Ka X-ray radiation during XPS analysis. The Raman spectra were measured on a LabRAM HR system with the excitation laser at λ=532 nm. Field emission scanning electron microscope (FESEM, JSM-5910LV, equipped with an energy dispersive Spectroscope, EDS) and field emission transmission electron microscopy (FETEM Tecnai G^2 F20 S-TWIN) were used to examine the morphology and crystalline structure of the samples. Nitrogen sorption isotherms were measured at 77.3 K after being degassed at 300 ℃ for 3 h (Micrometrics ASAP-2020 adsorption apparatus). The specific surface area and pore size distribution of the samples were derived using the multipoint Braunauer-Emmett-Teller (BET) method and the Barrett-Joyner-Halenda (BJH) model, respectively. The elemental content of Li in LTO-RTO was analyzed by atomic absorption spectroscopy (AAS, SpectrAA 220FS); thus the amount of LTO can be estimated.

To analyze the changes of the electrode surface morphology, the cycled and fresh coin cells were dissembled in a glove box under Ar atmosphere, and the electrodes were rinsed with alcohol and dried before analysis.

2.3 Electrochemical characterization

To fabricate the working electrodes, the synthesized samples, polyvinylidene fluoride (PVDF) binder and acetylene black were respectively mixed together at a weight ratio of 80:10:10 in solvent N-methyl-2-pyrrolidone. The obtained slurry was then pasted uniformly on a pure copper foil current collector; its thickness is 14 μm. After drying in air at 80 °C for 12 h, the foil was punched into 14 mm diameter wafers. The typical mass load of dry slurry was about 2 mg cm^{-2}. The electrochemical characters were carried out with CR2025 type cells, which were assembled in an argon-filled glove box (O_2 < 10 ppm, H_2O < 10 ppm) by using pure lithium foil as negative electrode, the prepared working electrode as positive electrode, 1 mm thick stainless steel as gasket, Celgard 2500 polypropylene film as separator, and a solution of 1M $LiPF_6$ in ethylene carbonate and dimethyl carbonate (EC+DMC, 1:1 in volume) as electrolyte. The test cells were galvanostatically discharged/charged under different current densities between 1.0 and 2.5 V (vs. Li/Li^+) using a LAND cell test 2001A system (Wuhan Jinnuo, China).

3 Results and discussion

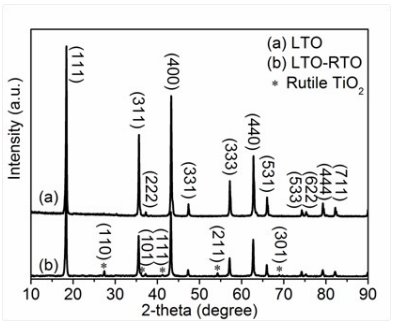

Fig.1. XRD patterns of the as-prepared samples: (a) LTO and (b) LTO–RTO (*) denote the XRD peaks of rutile TiO_2.

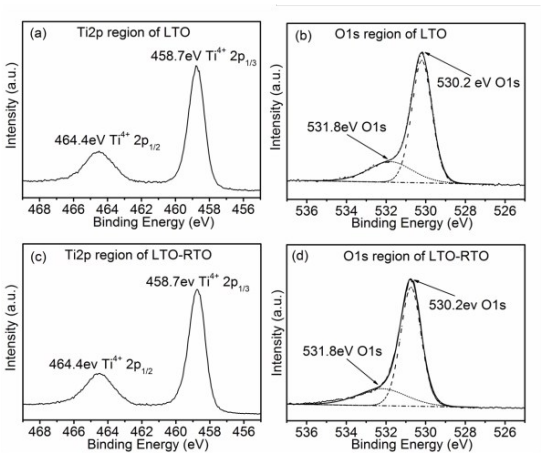

Fig. 2 XPS high-resolution spectra of the (a) Ti2p of LTO, (b) O1s of LTO, (c) Ti2p of LTO-RTO, and (d) O1s of LTO-RTO.

Figure 1 shows the X-ray diffraction patterns of the as-prepared two samples synthesized with different amount of LiOH·H_2O and calcinated at 600 ℃ for 10 h in air. All the diffraction peaks of the sample [Fig. 1(a)] can be indexed well to the cubic spinel LTO structure (JCPDS, No. 49-0207). As shown in Fig. 1(b), in addition to strong peaks of cubic spinel phase LTO (JCPDS Card No. 49-0207), some relatively small peaks corresponding to the RTO (JCPDS, No. 87-0920) are also observed at 2θ = 27.45°, 36.08°, 41.22°, 54.32°, and 68.9°. Atomic absorption spectroscopy (AAS) elemental analyses reveal 5.5 wt% Li in the LTO–RTO composite; thus, the amount of RTO in the composite is approximately 8.86 wt%.

X-ray photoelectron spectroscopy (XPS) was conducted to get the surface information of LTO and LTO-RTO samples, and there high-resolution of Ti2p and O1s binding energy regions were shown in Fig. 2. As shown in Fig. 2(a) and 2(c), both samples present a $Ti2p_{1/2}$ peak centered at around 464.4 eV and a $Ti2p_{3/2}$ peak at 458.7 eV, indicating that the oxidation state of the Ti cations is mainly Ti^{4+}, in good consensus with the valence of titanium in LTO and RTO.[31] The O1s photoelectron spectra of LTO and LTO-RTO are compared in Fig. 2(b) and 2(d). Both spectra exhibit the main peak at a binding energy of 530.2 eV, which can be derived from oxygen associated to Ti-O in the synthesized materials. The peaks at 531.8 eV can be attributed to oxygen and water molecules absorbed on the surface of the materials.[32] Although both samples XPS spectra are similar to each other, the great difference is revealed by calculation the mol ratio of O and Ti atoms. For the LTO, the calculated mol ratio of O : Ti is about 2.403 (For O1s, just using the peak area at 530.2 eV), which is very close to the theoretical value of pure LTO (O : Ti = 2.4). However, this value of LTO-RTO is about 2.266, indicating that the amount of RTO (O : Ti = 2) in LTO-RTO composite is about 8.84 wt%. This value is in good accordance with the result analysed by AAS method, which suggests that the in situ generated RTO is evenly distributed in LTO-RTO nanocomposite.

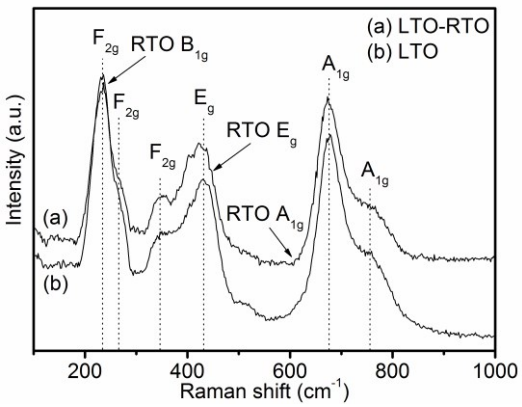

Fig. 3 Raman spectra of (a) LTO-RTO and (b) LTO

Raman spectra of obtained LTO and LTO-RTO samples are presented in Fig. 3. As we see, both samples show typical spinel structure features with all five active Raman phonon modes (A_{1g} + E_g + $3F_{2g}$), indicating the phase of cubic spinel LTO.[33] The higher frequency peak at 678 cm^{-1} (A_{1g}) with a shoulder at 753 cm^{-1} can be assigned to the vibrations of Ti-O bonds in TiO_6 octahedra. The middle frequency peak at 431 cm^{-1} can be attributed to the stretching vibrational mode of Li-O bonds in LiO_4 tetrahedra (E_g). Three lower frequency peaks (F_{2g}) at 340 cm^{-1}, 268 cm^{-1} and 234 cm^{-1} are originated from the vibration of Li-O bounds. However, no obvious RTO peaks are observed in the LTO-RTO sample, but the width of peaks are wider than that of LTO sample. The reasons can be attributed to the relative small amount of RTO and that the peaks position of RTO and LTO are close to each other (as shown in Fig. 3), thus leading to these peaks overlap together. Similar phenomenon was also found in previous reported Ag doped LTO.[33]

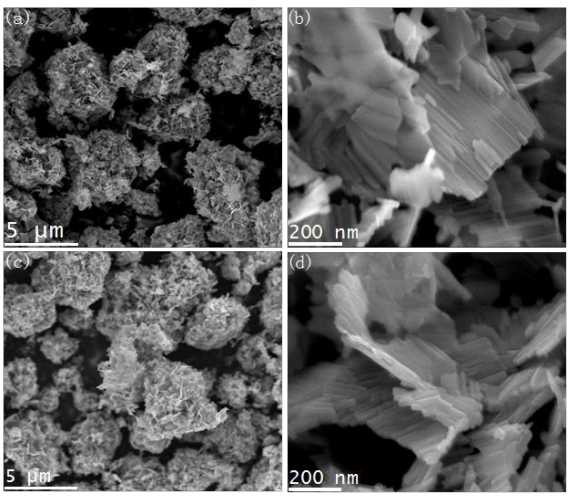

Fig.4 FESEM images of as-prepared samples: (a-b) LTO and (c-d) LTO–RTO.

The morphologies of as-prepared LTO and LTO–RTO samples were characterized by FESEM. At low magnification, both the LTO and LTO–RTO samples consist of flower-like particles with a similar equivalent diameter of about 3 μm to 4 μm [Fig. 4(a) and 4(c)]. At higher magnification [Fig. 4(b) and 4(d)], one can see that these flower-like particles have a lamellar structure stacked by the primary nanosheets. The thickness of primary nanosheet is in the range of about 10 nm to 30 nm. Comparing the FESEM images of LTO and LTO-RTO, no considerable differences in morphology and particle size are found between the samples, probably because the same preparation process is used.

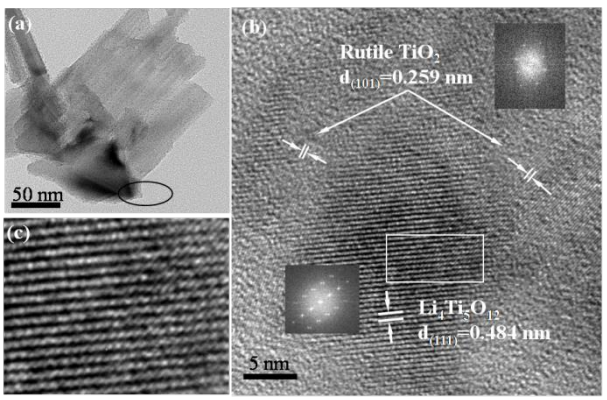

Fig.5 TEM (a) and HRTEM (b, c) images of LTO–RTO ((b) corresponds to elliptical region of (a), and (c) corresponds to rectangular region of (b).).

To understand the distribution of RTO in the LTO–RTO composite, the detailed structure of LTO–RTO sample was investigated by FETEM. The HRTEM image of ellipse area located in Fig. 5(a) is shown in Fig. 5(b), which indicates two sets of lattice fringes arranged in different directions. These fringes are indexed and calibrated to lattice spacing d = 0.259 and 0.484 nm, which correspond to the (101) plane of RTO and (111) plane of LTO, respectively. The corresponding fast Fourier transformation (FFT) images show glowing bright spots arranged in two different symmetrical patterns, indicating that the formation of LTO–RTO composite is highly crystallized. There are no distinct boundary and lattice distortion between phase LTO and RTO, moreover, in the cross-over region of two phase lattice [the rectangle area in Fig. 5(b)], we can still see the separate lattice fringes of LTO and RTO [Fig.5 (c)]. Obviously, nanosized RTO sheets are in situ grown on the LTO nanosheet. However, in the case of LTO sample, the laminated structure is only stacked by LTO nanosheets.

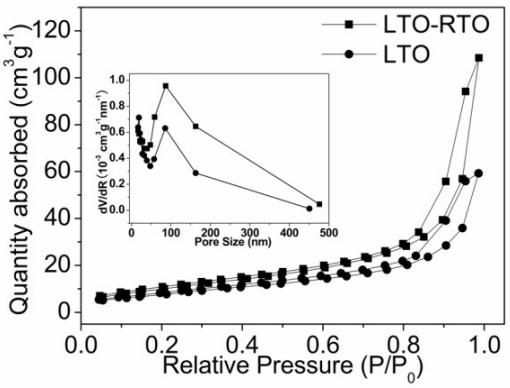

Fig.6 The N_2 adsorption/desorption isotherm of LTO and LTO–RTO; the inset shows the corresponding pore size distributions of LTO and LTO–RTO.

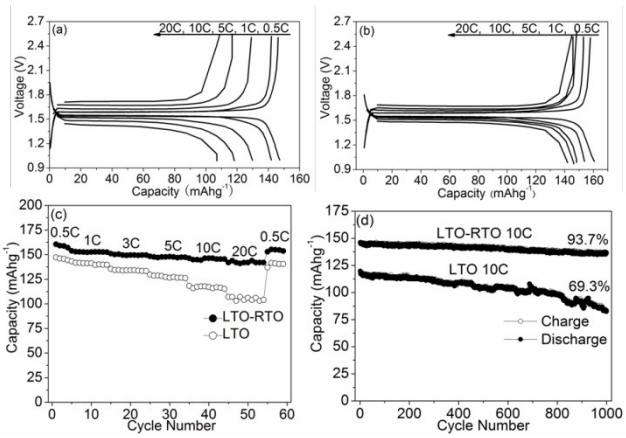

Fig.7 Galvanostatic charge/discharge profiles of (a) LTO and (b) LTO–RTO at different rates from 0.5 to 20 C. (c) Comparison of the rate capabilities of LTO and LTO-RTO electrodes and (d) cyclic performance of the LTO–RTO and LTO electrodes at a charge/discharge rate of 10 C.

Fig. 6 shows the the N_2 adsorption/desorption and pore size distribution (the inset in Fig. 6) curves of LTO and LTO–RTO samples, which were studied by nitrogen adsorption/desorption isotherms at 77.3 K after being degassed at 300 ℃ for 3 h. As shown in Fig.6, both samples display a typical type-IV isotherm with a clear H3 hysteresis loop, suggesting the existence of slit-shaped pores in the products. Based on the adsorption/desorption isotherms, the calculated BET specific surface area and BJH average pore radius of the LTO–RTO (85.8 nm and 39.1 m^2g^{-1}, respectively) are slightly higher than those of LTO (61.4 nm and 29.9 m^2g^{-1}, respectively). Such a flower-like particle with relatively large open slit pores created by the stacked nanosheets allows easily penetration of the electrolyte into the active material.

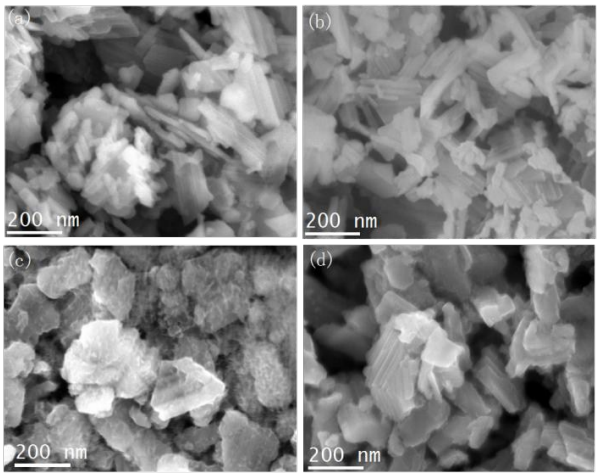

Fig.8 FESEM images of (a) LTO and (b) LTO–RTO electrodes after 1000 cycles at a charge/discharge rate of 10C.

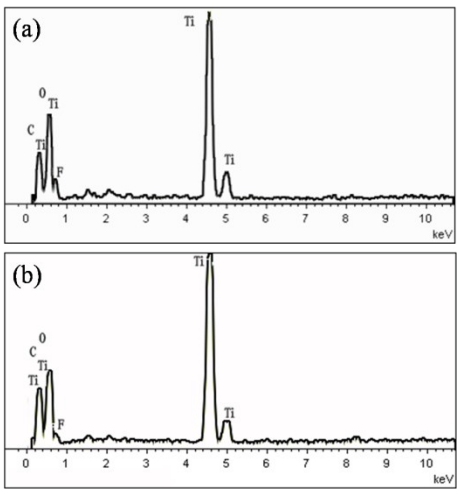

Fig. 9 EDX spectra of electrodes after 1000 cycles at 10 C: (a) LTO, (b) LTO-RTO.

The electrochemical behavior of LTO–RTO was systematically investigated and compared with that of LTO. The galvanostatic charge/discharge voltage profiles of two electrodes obtained at various current rates from 0.5 C to 20 C (1 C=175mA h g^{-1}) are presented in Fig. 7(a) and 7(b), respectively. At low current rate (0.5 C), flat discharge plateaus are observed at approximately 1.54 V in both electrodes, which correspond to the extraction of lithium ions from the LTO phase. With the increase in applied current density from 0.5 C to 1, 5, 10 and 20 C, the discharge

capacity of LTO declines quickly from the original 147 mA h g^{-1} to 142, 130, 118, and 107 mA h g^{-1}, respectively. In contrast, the LTO–RTO demonstrates slower capacity decay accompanied by much smaller polarization, such that even at high C-rates of 5, 10, and 20 C, capacities of 148, 146, and 142 mA h g^{-1} (the capacities are calculated based on the total weight of the LTO and RTO in the LTO–RTO electrode) are still retained with long and flat plateaus. This high rate capability is much better than those of previously reported LTO-anatase TiO_2 composites with capacity no more than 130 mA h g^{-1}.[11, 21-23] Besides, the differences between the potentials of charge and discharge plateaus of LTO (△E) increase much faster than that of LTO–RTO with increasing C-rate (See supporting information, Fig. S1), indicating the serious polarization of LTO electrode. The rate performance of LTO–RTO and LTO electrodes at different discharge/charge rates are compared in Fig. 7(c). The LTO–RTO electrode exhibits a significantly higher capacity and considerably better rate capability than the LTO electrode.

Table 1 Comparison cycling performance of LTO-RTO with other LTO based high-rate electrodes reported recently (Discharge range: 2.5-1.0 V).

Samples	Cycling performance	
	Capacity/mAhg^{-1}	Retention/%
LTO-anatase TiO_2[11]	110 after 100 cycles at 5 C	85
LTO-anatase TiO_2[21]	125 after 100 cycles at 10 C	98
LTO-anatase TiO_2[22]	118 after 100 cycles at 10 C	93
LTO-anatase TiO_2-C[13]	110 after 100 cycles at 10 C	82
LTO-anatase TiO_2[23]	117 after 300 cycles at 1 C	63
Au coated LTO[34]	154 after 100 cycles at 5 C	91
$LiCrTiO_4$/MWCNT[35]	115 after 200 cycles at 10 C	96
Carbon coated LTO[36]	104 after 500 cycles at 10 C	90
Mesoporous LTO[37]	120 after 300 cycles at 5 C	88
LTO nanoclusters[38]	122 after 100 cycles at 5 C	88
Mesoporous LTO[39]	144 after 200 cycles at 10 C	91
Core-shell LTO[40]	131 after 1000 cycles at 10 C	95
Cu^{2+} doped LTO[41]	112 after 100 cycles at 10 C	98
La-doped LTO[42]	140 after 1000 cycles at 10 C	90
Present work	144 after 100 cycles at 10 C	98.6
	141 after 500 cycles at 10 C	96.6
	137 after 1000 cycles at 10 C	93.7

The most attractive performance of LTO–RTO nanosheet composite is the outstanding long-term cycling stability at high rate current. As shown in Fig. 7(d), even after 1000 discharge/charge cycles at rate of 10 C, the LTO–RTO electrode still delivers capacity as high as 137 mA h g^{-1} with capacity retention of 93.7%. In contrast, the discharge capacity of pure LTO nanosheet drops rapidly to 83.1 mAh g^{-1} after 1000 discharge/charge cycles at the same rate, and the corresponding capacity retention is only 69.3%. We also compared the current work with other LTO-based high-rate electrodes in previous studies, including LTO–anatase TiO_2 composites,[11, 13, 21–24] surface modified LTO,[35–37] nanostructured LTO,[38–41] ion-doped LTO,[42–43] and these results are shown in Table 1. By comparison, the high-rate cycling performance of the LTO–RTO electrode is comparable to that of the La-doped LTO and remarkably better than those of other LTO-based electrodes. Importantly, our synthesis process is very simple and convenient, which is suitable for large scale production.

To get an insight into the superior cycling stability of LTO–RTO electrode, the LTO and LTO–RTO electrodes before and after 1000 cycles at 10 C were respectively dissembled from fresh and cycled (1000 cycles at 10 C) cells in a glove box under Ar atmosphere and rinsed with alcohol with several times. After drying, these electrodes were taken out and characterized by FESEM, as shown in Fig. 8. Comparing Fig. 8(a) and 8(c), we can clearly see that great changes have taken place in microstructure of LTO electrode after long-term cycling. The layer-stacked LTO nanosheets are covered by some nebulous substance, and the lamellar structures become indistinct. It is this nebulous substance that blocks the slit pores for the infiltration of electrode and hinders the transfer of Li ions and electrons, leading to the fast fading of capacity. Besides, original stacked thin LTO nanosheets were agglomerated into thicker sheets or larger particles. The similar phenomenon was also found in previous reported nano-structured electrode material.[43] However, in the case of LTO–RTO electrode, the laminated structures were still maintained clearly, even though they have undergone a thousand lithium ions intercalation and deintercalation cycles. To further analyze the surface compositions of cycled LTO and LTO-RTO electrodes (after 1000 cycles at 10 C), the energy dispersive X-ray spectroscopy (EDS) was carried out. As shown in Fig. 9, additional fluorine (F) element, but without P element, is found on the surface of both cycled electrodes, however, the weight rate of F element on LTO electrode (13.69%) is much higher than that of LTO-RTO electrode (5.42%). According to the previous research, the F element comes from the decomposition of $LiPF_6$ in electrolyte.[44] We think that the nebulous substance covered on the cycled LTO nanosheets is the product of side reactions with electrolyte. So, we can infer that the in situ generated nanosized RTO sheets in the LTO-RTO electrode may play an important role in inhibiting the occurrence of side reactions during long-term electrochemical charge/discharge cycling. However, the mechanism is still unclear, and more work needs to be carried out.

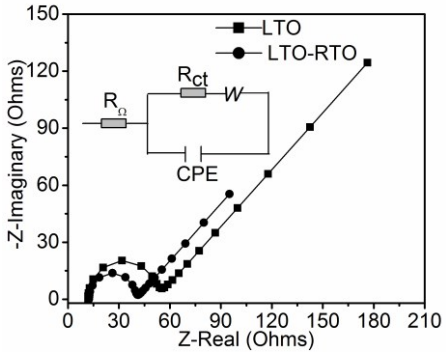

Fig.10 Nyquist plots of LTO and LTO–RTO electrodes after 5 cycles at 0.5 C.

In order to further understand the effect of in situ generated RTO nanosheets on the electrochemical performance of LTO–RTO electrode, the electrochemical impedance spectroscopy (EIS) was employed to identify the relationship between the electrode kinetics and electrochemical performance. The Nyquist plots of

the LTO and LTO–RTO electrodes obtained at open-circuit voltages after initial 5 cycles (0.5 C) as well as the fitting results using an equivalent circuit are depicted in Fig. 10. It can be seen that the Nyquist plots of both electrodes are comprised of a depressed semicircle from high to medium frequency and a linear Warburg region (*W*) at low frequency. It is well known that the intercept value of impedance spectra on the real *Z* axis at the high frequency is the internal resistance, including the resistance of the electrode/electrolyte interface, separator, and electrical contacts, which corresponds to the ohmic resistance (R_{Ω}) in the equivalent circuit.[20] The similar R_{Ω} for both cells is anticipated since they used the same electrolyte, separator, and same content conductive additive. The semicircle from high to medium frequency is associated with the charge-transfer resistance (R_{ct}) related to lithium-ion interfacial transfer, coupled with constant phase-angle element (*CPE*).[13] It can be clearly seen that the values of R_{ct} for both electrodes are lower than 45 Ω, owing to the nanosheet morphology greatly shortens the diffusion lengths for both Li ions and electrons. However, the R_{ct} of LTO–RTO (R_{ct} = 27 Ω) is much smaller than that of LTO (R_{ct}=40 Ω), indicating that the sandwich structures could enable much easier charge transfer at the electrode/electrolyte interface. Furthermore, the exchange current density could also be calculated from the equation of $i^0 = RT/nFR_{ct}$.[45] In this way, the charge-transfer kinetics of LTO–RTO electrode (i^0 = 0.94 mA cm^{-2}) is nearly 1.5 times of LTO electrode (i^0 = 0.63 mA cm^{-2}).

This enhanced kinetics and superior electrochemical performances of the LTO–RTO sample could be explained as follows. Firstly, nanosheets assembled flower-like particles possess numerous open slit-pores, which ensure good penetration of the active material by the electrolyte, and thus shorten the lithium ions diffusion length. Secondly, it has been reported that grain boundaries and interfacial areas between the two phases in a composite sample, are favorable for decreasing the charge transfer resistance via interfacial storage mechanism,[13, 20] and hence they enhance the rate capability. In the LTO-RTO nanocomposite, RTO nanosheetes are in situ grown on the LTO nanosheets, producing a large number of LTO/RTO two-phase interfaces. These interface areas can serve as tiny reaction sites for rapid lithium intercalation and extraction by significantly reducing the diffusion length of the Li ions,[13, 17–18, 20] thereby decreasing the charge transfer resistance and improving the rate performance. Thirdly, RTO is known to be active when it is nanosized material. On the one hand, nanoscaled RTO particles have higher capacity than LTO, so in situ generated RTO nanosheets can improve the overall composite capacity. On the other hand, Li^+ can insert RTO during the discharge process at 1.7 V (vs. Li^+/Li), forming the lithiated RTO, rutile-Li_xTiO_2. However, it has been proved that anatase TiO_2 in LTO/anatase - TiO_2 could improve the conductivity, due to the in situ formed anatase - Li_xTiO_2 during the discharge process. So, we infer that rutile-Li_xTiO_2 might also enhance the LTO/RTO electrode electrical conductivity. If so, in situ generated RTO nanosheets not only contribute capacity, but also indirectly improve the electrode conductivity, which are similar to the RuO_2 played roles in the TiO_2:RuO_2 composite electrode.[46] Fourthly, the in situ generated RTO nanosheets can effectively depress the side reactions and keep the integrity of lamellar structures during the long-term lithium ions intercalation and deintercalation process, thereby ensuring the excellent cycling stability. The high capacity, high rate capability, and excellent high rate long-term cycling stability of LTO–RTO electrode can be attributed to the synergetic effect of these positive factors.

Conclusions

$Li_4Ti_5O_{12}$–rutile TiO_2 nanocomposite with flower-like morphology was synthesized via a facile sol-hydrothermal synthesis method using LiOH·H_2O and $Ti(OC_4H_9)_4$ as precursors. The as-prepared $Li_4Ti_5O_{12}$–rutile TiO_2 flower-like particles possess numerous open slit-pores, which ensure good penetration of active material by the electrolyte. The layer-stacked nanosheets with a thickness of 10−30 nm significantly shorten the diffusion lengths for both Li ions and electrons. Furthermore, the in situ generated rutile TiO_2 nanosheets play important roles in providing large areas of $Li_4Ti_5O_{12}$ / rutile TiO_2 two-phase interface that serve as tiny reaction sites for reactions of Li^+ ions insertion/extraction, inhibiting occurrence of side reactions and avoiding aggregation of stacked $Li_4Ti_5O_{12}$ nanosheets during the Li^+ intercalation and deintercalation process. Benefiting from the synergetic effect of these positive factors, the as-prepared $Li_4Ti_5O_{12}$–rutile TiO_2 nanocomposite simultaneously achieved high rate capability (a reversible capacity of 148, 146 and 142 mA h g^{-1} at 5, 10 and 20 C, respectively) and as well as outstanding long-term cycling stability at high rate (only 6.3% capacity loss after 1000 cycles at a high current rate of 10 C with capacity retention of 137 mA h g^{-1}).

Notes and references

* College of Materials Science and Engineering, Sichuan University, No. 24 South Section 1, Yihuan Road, Chengdu , China, 610065; E-mail: maojian@scu.edu.cn

1 H.Q. Li and H.S. Zhou, *Chem. Commun.*, 2012, **48**, 1201–1217.
2 B.B. Tian, H.F. Xiang, L. Zheng, Z. Li and H.H. Wang, *Electrochim. Acta*, 2010, **55,** 5453–5458.
3 M. Winter and J.O. Besenhard, *Electrochim. Acta*, 1999, **45**, 31–50.
4 S. Flandrois and B. Simon, *Carbon*, 1999, **37**, 165–180.
5 C.Y. Ouyang, Z.Y. Zhong and M.S. Lei, *Electrochem. Commun.*, 2007, **9**, 1107–1112.
6 M. Kundu, S. Mahanty and R.N. Basu, *Mater. Lett.*, 2011, **65**, 1105–1107.
7 M. Park, K. Kim, J. Kim and J. Cho, *Adv. Mater.*, 2010, **22**, 415–418.
8 Y. Ma, C. Zhang, G. Ji and J.Y. Lee, *J. Mater. Chem.*, 2012, **22**, 7845–7850.
9 Y.F. Yuan, J.P. Tu, H.M. Wu, Y. Li and D.Q. Shi, *Nanotechnology*, 2005, **16**, 803–808.
10 M. Samiee and J. Luo, *J. Power Sources* 2014, **245**, 594–598.
11 J. Wang, H.L. Zhao, Q. Yang, C. Wang, P. Lv and Q. Xia, *J. Power Sources*, 2013, **2229**, 196–201.
12 T. Ohzuku, A. Ueda and N. Yamamoto, *J. Electrochem. Soc.*, 1995, **142**, 1431–1435.
13 M.M. Rahman, J.Z. Wang, M.F. Hassan, D. Wexler and H.K. Liu, *Adv. Energy Mater.*, 2011, **1**, 212–220.
14 M.S. Song, R.H. Kim, S.W. Baek, K.S. Lee, K. Park and A. Benayad, *J. Mater. Chem. A*, 2014, **2**, 63–636.
15 L. Zhao , Y.S. Hu , H. Li, Z. Wang and L. Chen, *Adv. Mater.*, 2011, **23**, 1385–1388.
16 Y.H. Rho and K. Kanamura, *J. Solid State Chem.*, 2004, **177**, 2094–2100.
17 S. Grugeon, S. Laruelle, R. Herrera-Urbina, L. Dupont, P. Poizot and J.M. Tarascon, *J. Electrochem. Soc.*, 2001, **148**, A285–A292.
18 H. Li and G. Richter, J. Maier, *Adv. Mater.*, 2003, **15**, 736–739.

19 L.Y. Beaulieu and J.R. Dahn, *J. Electrochem.Soc*., 2000, **147**, 3237–3241.

20 G.N. Zhu, L. Chen, Y.G. Wang, C.X. Wang, R.C. Che and Y.Y. Xia, *Adv. Funct. Mater.*, 2013, **23**, 640–647.

21 F.X. Wu, X.H. Li, Z.X. Wang and H.J. Guo, *Nanoscale*, 2013, **5**, 6936–6943.

22 J.Y. Liao, X. Xiao, D. Higgins, D. Lee F. Hassan and Z. Chen, *Electrochim. Acta*, 2013, **108**, 104–111.

23 X. Li, C. Lai, C.W. Xiao and X.P. Gao, *Electrochim. Acta*, 2011, **56**, 9152–9158.

24 X.-P. Li and J. Mao, *Ceram. Int.*, 2014, **40**, 13553–13558.

25 J. Chen, L. Yang, S. Fang and Y. Tang, *Electrochim. Acta* 2010, **55**, 6596–6600.

26 J.S. Chen and X.W. Lou, materialstoday, 2012, **15**, 246–254.

27 X.-G. Han, Q. Kuang, M.-S. Jin, Z.-X. Xie and L.-S. Zheng, *J. Am. Chem. Soc*., 2009, **131**, 3152–3153.

28 Y.Q. Wang, L. Gu, Y.G. Guo, H. Li, X.Q. He, S. Tsukimoto, Y. Ikuhara, L.J. Wan, *J. Am. Chem. Soc.* 2012, **134**, 7874–7879.

29 B. Mao, Z. Kang, E. Wang, S. Lian, L. Gao, C. Tian and C. Wang, *Mater. Res. Bull*., 2006, **41**, 2226–2231.

30 H. Yu, H. Zhang, H. Huang, Y. Liu, H. Li, H. Ming and Z. Kang, *New J. Chem.*, 2012, **36**, 1031–1035.

31 J. Mosa, J.F. Vélez, J.J. Reinosa, M. Aparicio, A. Yamaguchi, K. Tadanaga and M. Tatsumisago, *J. Power Sources*, 2013, **244**, 482–487.

32 Z. Yang, Q. Meng, Z. Guo, X. Yu, T. Guo and R. Zeng, *Energy*, 2013, **55**, 925–932.

33 G.B. Xu, W. Li, L.W. Yang, X.L. Wei, J.W. Ding, J.X. Zhong, Paul K. Chu, *J. Power Sources*, 2015, **276**, 247–254.

34 W. Wang, Y. Guo, L. Liu, S. Wang, X. Yang and H. Guo, *J. Power Sources*, 2014, **245**, 624–629.

35 C. Lin, X. Fan, Y. Xin, F. Cheng, M.O. Lai, H. Zhou and L. Lu, *J. Mater. Chem. A*, 2014, **2**, 9982–9993.

36 E. Kang, Y.S. Jung, G. Kim, J. Chun, U. Wiesner, A.C. Dillon , J.K. Kim and J. Lee, *Adv. Funct. Mater*., 2011, **21**, 4349–4357.

37 L. Yu, H. B. Wu and X.W. Lou, *Adv. Mater*., 2013, **25**, 2296–2300.

38 L. Sun, J. Wang, K. Jiang and S. Fan, *J. Power Sources*, 2014, **248**, 265–272.

39 G. Du, Z. Liu, S.W. Tay, X. Liu and A. Yu, *Chem. Asian J*., 2014, **9**, 2514-2518.

40 L. Shen, H. Li, E. Uchaker, X. Zhang and G. Cao, *Nano Lett.*, 2012, **12**, 5673−5678.

41 C. Lin, B. Ding, Y. Xin, F. Cheng, M.O. Lai, L. Lu and H. Zhou, *J. Power Sources*, 2014, **248**, 1034–1041.

42 Y. Bai, C. Gong, Y. Qi, N. Lun and J. Feng, *J. Mater. Chem.*, 2012, **22**, 19054–19060.

43 H. Qiao, L. F. Xiao and L. Z. Zhang, *Electrochem. Commun.*, 2008, **10**, 616–620.

44 J. Demeaux, E.D. Vito, M.L. Digabel, H. Galiano,B. Claude-Montignybd and D. Lemordantbd, *Phys.Chem.Chem.Phys.*,2014, **16**, 5201–5212.

45 Y. Ma, B. Ding, G. Ji and J.Y. Lee, *ACS Nano*, 2013, **7**, 10870–10878.

46 Y.-G. Guo, Y.-S. Hu, W. Sigle and J. Maier, *Adv. Mater.*, **19**, 2007, 2087–2091.